Central collisions in the $^{16}O + ^{12}C$ reaction at 32.5 MeV/nucleon

J. A. Scarpaci,[1,2] Y. Chan,[1] D. DiGregorio,[1,3] B. A. Harmon,[1,4] J. Pouliot,[1,5] R. G. Stokstad,[1] and J. Suro[1,6]
[1]*Lawrence Berkeley Laboratory, Berkeley, California 94720*
[2]*Institut de Physique Nucléaire, 91406 Orsay Cedex, France*
[3]*Departamento de Física-TANDAR, Comisión National de Energía Atómica, 1429 Buenos Aires, Argentina and Conicet*
[4]*Space Science Laboratory, Nasa/Marshall Space Flight Center, Huntsville, Alabama 35812*
[5]*Laboratoire de Physique Nucléaire, Université Laval, Québec, P.Q., Canada G1K 7P4*
[6]*Instituto de Física, Universidad Nacional Autónoma de México, Apartado Postal 20364, México 01000 D.F., Mexico*
(Received 24 January 1995)

Central collisions of ^{16}O on a ^{12}C target have been studied at 32.5 MeV/A. An analysis in terms of incomplete fusion followed by statistical decay is presented and the main channels for the incomplete fusion are extracted for this reaction. A detailed study of the specific channel, 5He+2H, shows a good agreement with a statistical decay of the ^{24}Mg parent nucleus while a multifragmentation model predicts a larger sphericity for these events.

PACS number(s): 25.70.Mn

I. INTRODUCTION

Breakup studies of light nuclei such as ^{16}O and ^{20}Ne in peripheral reactions [1] have shown consistency with a statistical decay process. In these inelastic collisions the system undergoes a relatively gentle reaction, which could be the reason for the apparent equilibration decay. In order to search for nonequilibrium phenomena, we studied central collisions where hotter nuclei are formed. We chose a relatively light system ^{16}O beam at 32.5 MeV/nucleon of incident energy on a ^{12}C target and selected central collisions by requiring a large multiplicity of fragments in the multielement detector used to observe the reaction.

After a description of the experimental apparatus, we present an analysis of the center of mass velocity to determine the main composite nuclei formed through incomplete fusion. We then examine in detail a channel in which a large number of particles and large total charge is detected, the 5He+2H channel. A sphericity and coplanarity of the events are determined and compared with simulations.

II. EXPERIMENT

The experiment was performed at the LBL 88-inch Cyclotron and the detection system (Fig. 1) consisted of an array of 48 truncated pyramidal (TP) plastic phoswich detectors covering the forward angles from 2.5° to 17.5° [2] and 10 position-sensitive plastic phoswich detectors [3], covering larger angles up to 78° in the horizontal direction and 56° in the vertical direction. All plastic detectors were of the ΔE-E type and had a 0.4 mm thick fast scintillator (BC-404) for the ΔE element and a slow scintillator (NE-115) for the E element. The E element in a TP detector was 10.2 cm thick and could stop protons up to 100 MeV. In the position-sensitive detectors the E element was 2.5 cm thick. The thresholds for particle identification ranged from 8 MeV for protons to 10 MeV per nucleon for Be, B, and C.

For a TP detector three values were recorded for every detected particle: a "short gate" value ($\mathcal{S}_\mathcal{G}$), which was the fast component of the output signal integrated in a 40 ns gate, a "long gate" value ($\mathcal{L}_\mathcal{G}$), which was the integration of the total signal in a 2 μs gate, and a time signal. The short gate corresponded approximately to the energy deposited in the ΔE element and the long gate approximately to the total energy. For a position-sensitive detector, five values were recorded: two $\mathcal{S}_\mathcal{G}$ values and two $\mathcal{L}_\mathcal{G}$ values, one for each end of the detector,

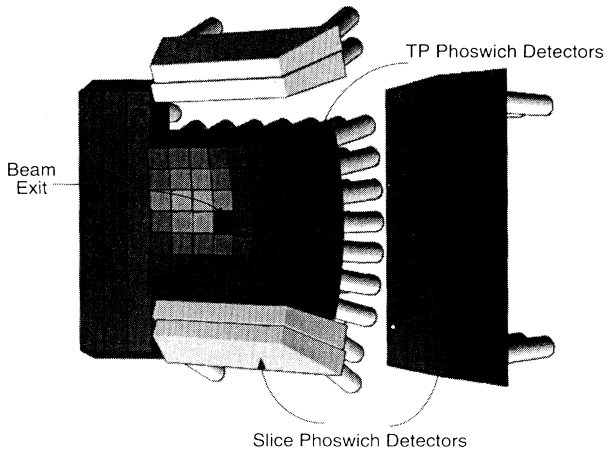

FIG. 1. Plastic phoswich detector array for light charged particles. The slices are positioned symmetrically about the 47-detector array. The top and right slice detectors have been shifted in the drawing to reveal the central cubic array.

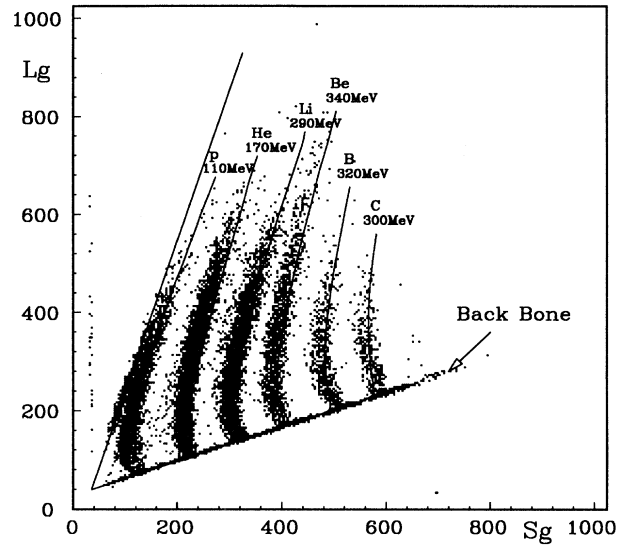

FIG. 2. Particle identification spectrum obtained with a truncated pyramidal detector. The solid lines are the results of a calculation used in the energy calibration procedure.

and the time signal.

A typical ΔE-E identification spectrum for a TP detector is shown is Fig. 2. The coordinates are the $\mathcal{L}_\mathcal{G}$ and the $\mathcal{S}_\mathcal{G}$ signals. Similar plots were obtained for the position- sensitive detector, as described in Ref. [3]. Fragments up to carbon are seen and the adjacent charge lines are well separated. The lower straight line, or "backbone," corresponds to particles that were stopped in the ΔE scintillator. The upper straight line corresponds to the relatively few particles that missed the ΔE layer but deposited energy in the E detector. Particles in either of these lines could not be identified.

The detectors were calibrated by using several different beams at 32.5 MeV per nucleon and a series of degraders in order to obtain energies varying from 14 to 65 MeV for deuterons, 74 to 139 MeV for alpha particles, and 262 to 390 MeV for ^{12}C. These beams were then elastically scattered by a thin gold target, giving a series of energy calibration points for several particle identification lines in Fig. 2.

The calibration points and the loci of the lines in Fig. 2 were fit with a generic function that described the responses of the detectors. An agreement of about 2% in energy for protons and better than 10% for carbon ions was obtained when individual calibration points for the set of all detectors were compared with the energies deduced from fitting all the calibration points and the loci of the identification lines. The details of this calibration procedure are described in the Appendix.

III. ANALYSIS OF THE DATA IN TERMS OF INCOMPLETE FUSION FOLLOWED BY STATISTICAL DECAY

In our earlier experiment on peripheral reactions involving a light projectile on a heavy target [4], the emitting nucleus was the excited projectile or a nucleus with mass very close to that of the projectile. In a central collision at energies over 10–20 MeV/A, however, the emitting nucleus is not as well defined. Incomplete fusion, a process in which only a portion of one of the reaction partners fuses with all or a portion of the other reaction partner, can produce, in our reaction, a range of primary composite nuclei varying from oxygen to silicon. Furthermore, our detector did not cover the full solid angle, which made it more difficult to characterize the primary nuclei. For example, the detection of a total of 12 charges in an event does not necessarily imply that the primary nucleus was magnesium. It could have been aluminum or silicon, and some charges either missed the array or may have had too small an energy to be identified. Therefore it is necessary first to unravel the different primary nuclei that produced the final measured channels.

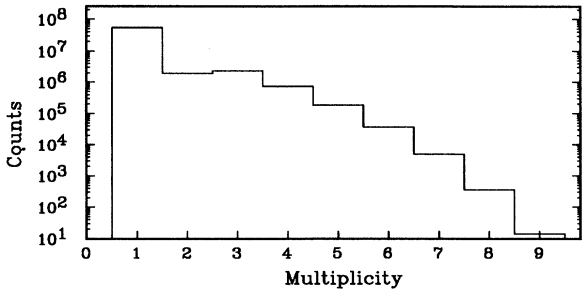

FIG. 3. Multiplicity distribution obtained in a measurement with the trigger level set at one detector.

A. Experimental velocity distribution

An electronic multiplicity threshold was set at six particles in order to enhance the central collision events during data taking. The multiplicity distribution without any threshold is shown in Fig. 3. Figure 4 shows the distribution of the total detected charge ($Z_{\rm det}$) with and without the multiplicity threshold. Note the strong (and expected) correlation between high multiplicity and high total detected charge. Our analysis included only those channels having multiplicity ≥ 6.

Each event was characterized by the total amount of

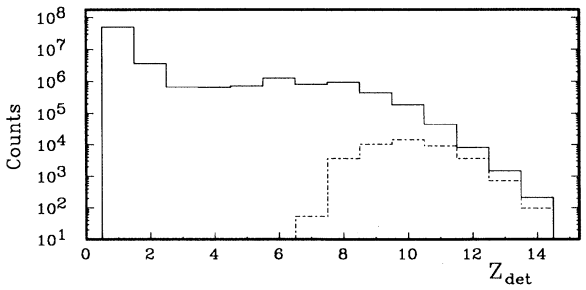

FIG. 4. Total detected charge distribution for all events (solid histogram) and for multiplicity higher or equal to 6 (dashed histogram).

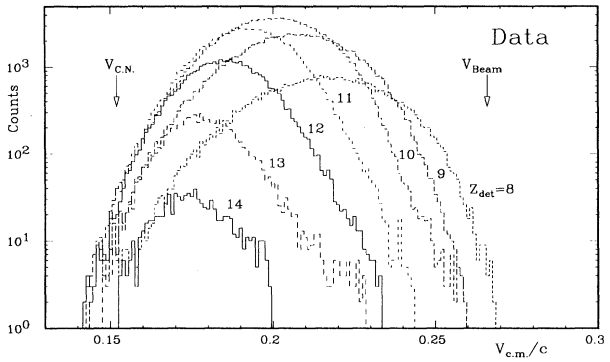

FIG. 5. Laboratory velocity spectra of the center of mass of the detected fragments for each total detected charge from 8 to 14. The beam velocity and the compound nucleus velocity are indicated by the arrows.

detected charge. Since isotopes could not be identified, we made the following assumptions about the masses of the particles. We took singly charged nuclei to be protons and doubly charged nuclei to be ^{4}He. For higher charges we assumed a mass equal to the most stable isotope. Note that it is not necessary to know the true masses of the fragments in each event in order to make comparison with events calculated in a Monte Carlo simulation; it is only necessary to make the same assumptions in analyzing the simulated events as were made in analyzing the experimental events.

The velocity of the center of mass of the detected fragments was calculated and a velocity spectrum created for each set of events having the same total charge. Experimental spectra are shown in Fig. 5, where the beam velocity and the compound nucleus (^{28}Si) velocity are also indicated. Note that the higher the total detected charge, the lower the center of mass velocity. This trend is expected since the greater the total charge detected, the greater the mass that must have been captured by the projectile. The spectrum with a total detected charge of 8 has an average velocity much lower than the beam velocity, which shows that this channel was not produced by inelastic scattering of the projectile. The average velocity, however, is substantially larger than that of the compound nucleus ^{28}Si. This implies an incomplete fusion of the target with the projectile, giving rise to a heavier ejectile from which only eight charges are detected.

Although we would expect the average velocity for the spectrum of 14 detected charges to equal the velocity of the compound nucleus, ^{28}Si, Fig. 5 shows this is not the case. This spectrum is centered at a higher velocity because the detector thresholds favor the fast charged particles emitted in the forward direction, which implies backward emitted neutrons (which are not detected) and thus a higher center of mass velocity for the fragments detected. Thus only part of the mass is detected and it has a higher forward-going average velocity. The spectra for charges of 13 and less are also biased toward higher center of mass velocities because of the detector thresholds.

B. Incomplete fusion

We fit each velocity spectrum (for each total detected charge) with a sum of different primary nuclei, each of which produces an event in the experimental apparatus having that total detected charge. For example, to reproduce the velocity spectrum for a total detected charge of 9, we calculated the decay of F, Ne, Na, Mg, Al, and Si nuclei, each moving with a laboratory velocity appropriate for an incomplete fusion reaction. We simulated the geometry and thresholds of the detector system, and created, for each decaying parent nucleus, the velocity spectrum for events where nine charges were detected. We used those calculated spectra to fit the experimental spectrum by adjusting the relative numbers of different primary emitting nuclei.

The assumptions made in the calculations for incomplete fusion are as follows. First we assumed that the mass was transfered from the target to the projectile. The second assumption (which we verified by simulations) was that the target remnant was not detected. This reaction mechanism produces a primary nucleus in the laboratory frame with a velocity large enough that the emitted fragments have energies above the detector thresholds. Several simulations were performed in order to check for events where both the target and the projectile are excited and emit fragments. The simulations showed that only a tiny fraction of events with fragments coming from the target or from the projectile could contribute to the observed data. In the case of a ^{16}O with 60 MeV excitation energy and a ^{12}C target with 40 MeV excitation energy, the maximum contribution would occur for the $Z_{\rm det}$=9 channel (considering a multiplicity higher or equal to 6) at a velocity about 0.24c, improving very little the fit for that channel. For higher $Z_{\rm det}$ channels, almost nothing remains after the filtering. Other possibilities were looked at, like incomplete fusion plus excitation of the target, but the fragments emitted from the target would in no case be detected in measurable amounts. Also, for partial mass transfer from projectile to target, most of the final fragments have too low an energy to be detected. This does not mean that these later processes are not occurring or has a low probability, only that we cannot observe them with our detection system.

In principle, the primary ejectile formed through incomplete fusion could be anything between fluorine and silicon with an isotopic mass ranging from 17 to 28. However, to have a manageable set of parameters in the analysis, we chose one isotope per element, each having the same neutron to proton ratio ($A = 2^*Z$) as the target and the projectile: ^{18}F, ^{20}Ne, ^{22}Na, ^{24}Mg, ^{26}Al, and ^{28}Si.

The velocity and excitation energy of the primary nuclei ($V_{\rm pri}$ and $E^*_{\rm pri}$, respectively) are the ones given by the incomplete fusion of the projectile with part of the target, the target remnant remaining cold and at rest in the laboratory frame:

$$E^*_{\rm pri} = E_i \frac{\mathcal{M}_{\rm pri} - \mathcal{M}_i}{\mathcal{M}_{\rm pri}} + Q_{\rm reaction}, \quad (1)$$

$$V_{\rm pri} = V_i \frac{\mathcal{M}_i}{\mathcal{M}_{\rm pri}}, \quad (2)$$

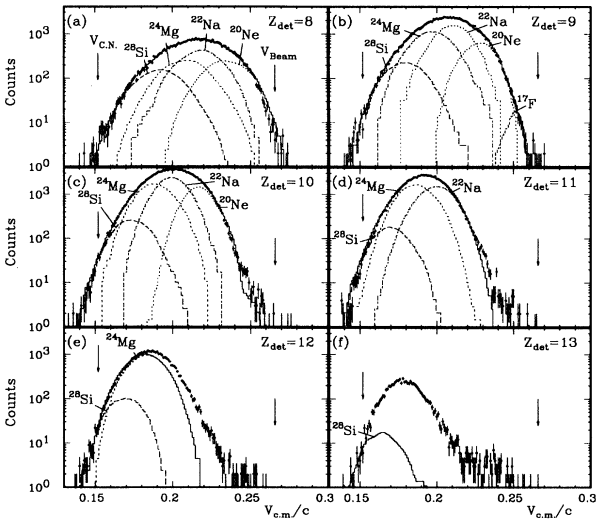

FIG. 6. Laboratory velocity spectra of each total detected charge fitted by GEMINI calculations performed with different primary nuclei.

where E_i is the projectile kinetic energy, $\mathcal{M}_i$ the projectile mass, $\mathcal{M}_{pri}$ the primary nucleus mass, and $Q_{reaction}$ is the Q value of the reaction. The maximum angular momentum of the composite system was calculated for the complete fusion of the projectile with a fraction of the target [5]. It ranges from $L_{max}=10$ for ^{18}F to $L_{max}=27$ for ^{28}Si. The total excitation energy obtained for ^{24}Mg formed through incomplete fusion is 180 MeV, according to the formulas given above, while the rotational energy for the maximum angular momentum of $l = 22\hbar$ would be around 60 MeV, leading to a temperature of about 6 MeV.

C. Statistical decay

Statistical model calculations have been performed with the Monte Carlo code GEMINI [6], which calculates the decay of a nucleus via a series of binary decays. All possible binary divisions of the system, from light particle emission to symmetric fission, are allowed at each decay step. For each fragment emitted in the decay of a primary nucleus, the laboratory energy was calculated by adding the center of mass motion of the emitting nucleus. Using the laboratory energy and the mass assumed for a fragment of that charge, the laboratory velocity of the fragment was calculated. Using the assumed masses and calculated velocities for individual fragments in an event, we calculated the velocity of the center of mass of the collection of fragments that struck detectors with energies above the detector threshold. This velocity for a calculated event was used in making a comparison with the experimental events shown in Fig. 5. We examined the consequences of making different assumptions in choosing the masses (e.g., in assuming singly charged nuclei to be protons) and found that these different asumptions did not change the conclusions drawn from comparing experiment and theory.

D. Comparison with the data

1. Distribution of primary nuclei

Each of the experimental velocity spectra shown in Fig. 5 was independently fit in the following manner, which we describe for a total detected charge of 10. The decay products calculated for each of the primary compound nuclei listed in the previous section were filtered through the experimental thresholds and geometry. Whenever the decay of a primary nucleus resulted in a total of ten (and only ten) charges passing the filter, i.e., in being "detected," the laboratory velocity of the center of mass of the fragments was calculated and an event added to the spectrum associated with that parent nucleus. The overall contribution from each primary nucleus that could contribute to the spectrum for $Z_{det}=10$ was then varied to achieve the best fit to that experimental spectrum. The result is shown in Fig. 6(c). The total number of

TABLE I. Total number of counts of the experimental data for a given Z_{det} as shown in Fig. 6 (Expt.). Same for the calculated contributions for each primary nucleus in the fit and for their sum (Simul.). The initial number of events needed for the fit before filtering is given in parentheses.

Z_{det}	Expt.	Simul.	^{28}Si	^{24}Mg	^{22}Na	^{20}Ne
8	36515	36463	5339	8954	13926	8244
			(1015000)	(1661000)	(5040000)	(4403000)
9	101615	101462	6876	35598	43456	15532
			(652000)	(1933000)	(3584000)	(1298000)
10	144091	144179	7251	46703	58153	32072
			(553000)	(2582000)	(1915000)	(1276000)
11	92199	92144	3360	46825	41959	-
			(454000)	(2205000)	(2878000)	(-)
12	36185	28826	2061	26765	-	-
			(518000)	(5904000)	(-)	(-)
13	7250	415	415	-	-	-
			(588000)	(-)	(-)	(-)
14	994	0	0	-	-	-
			(0)	(-)	(-)	(-)

TABLE II. Number of primary nuclei needed to fit the velocity spectrum of a given Z_{det} normalized to the $Z_{det}=9$ channel.

Z_{det}	^{28}Si	^{24}Mg	^{22}Na	^{20}Ne
8	1.55	0.86	1.40	3.39
9	1.00	1.00	1.00	1.00
10	0.85	0.83	0.53	0.98
11	0.70	1.14	0.80	—
12	0.79	3.46	—	—
13	0.90	—	—	—
14	0.00	—	—	—

experimental events was approximately 144 000 and was best fit with contributions of ~7300 events that passed the filter from the decay of ^{28}Si, ~46 700 from ^{24}Mg, ~58 200 from ^{22}Na, and ~32 100 from ^{20}Ne. This procedure was then repeated for each of the spectra shown in Fig. 6. The results are given in Table I, which also includes the number of primary nuclei that had to be produced in the incomplete fusion reaction in order to yield that number of detected events. No ^{18}F or ^{26}Al primary nuclei were needed to fit any of the spectra.

It should be possible in principle to deduce the relative population of primary nuclei produced in the incomplete fusion process (a reaction in which part of the ^{12}C target fuses with all of the projectile as explained in Sec. III B), by fitting a velocity spectrum for a single Z_{det}, which is populated by the decay of the heavier primary nuclei. The number of primary nuclei so deduced by fitting the velocity spectrum for $Z_{det}=9$ is given in parentheses in Table I. Therefore, a measure of the reliability of this analysis can be obtained by comparing the relative distribution of primary nuclei deduced from fitting each spectrum. This information is given in Table II, which gives the number of primary nuclei relative to the number deduced from fitting the experimental spectrum for $Z_{det}=9$. Complete consistency in the primary production ratios would result in the factor 1.0 everywhere in the table. A smaller number indicates that the fit to that spectrum required fewer primary nuclei than was found by fitting the spectrum for $Z_{det}=9$. In most cases the factors are close to 1 (especially where the contributions are large) and only in a few cases are they larger than 3. This gives us some confidence in using the incomplete fusion model to analyze the fusion of light nuclei at these high bombarding energies.

A summary of our understanding of the incomplete fusion reaction mechanism is presented in Table III, which is the best overall fit to the experimental data in Fig. 6. This table gives the distribution of primary nuclei produced in the reaction and the contributions they make to each spectrum for the different total detected charges. However, this distribution is affected by the detector filter and the minimum multiplicity of 6 required in the experiment. A more useful set of values would be the distribution of primary nuclei with no constraints on the multiplicity or on the detection system. This can be obtained from the number of primary nuclei used in the calculation to fit the spectra before applying any filtering. They are given in parenthesis in Table I and, as explained above, they should be identical for a given primary nucleus. One can average the values for the best fitted spectra, Z_{det} = 8–11, and extract a percentage of primary nuclei from the incomplete fusion. The results are given in Table III and show that the most probable nucleus obtained through incomplete fusion in the ^{16}O + ^{12}C reaction at 32.5 MeV/nucleon is ^{22}Na, with 40% of the cross section.

2. *Channel yields*

Additional checks on the reliability of this incomplete fusion analysis can be obtained by examining the distributions of charges obtained for the different channels having different total charges. For example, the following channels (all with multiplicity 6 or greater) can contribute to the spectrum for a total detected charge of 9: 3He+3H, Li+He+4H, 2He+5H, Be+5H, Li+6H, and He+7H. The intensity of the different channels depends on which primary nuclei contribute to the spectrum for

TABLE III. Distribution of primary nuclei produced in the reaction and the contributions they make to each spectrum for the different Z_{det}.

Z_{det}	% of the detected events	^{28}Si %	^{24}Mg %	^{22}Na %	^{20}Ne %	^{17}F %
8	8.7	1.3	2.1	3.3	2.0	0.0
9	24.3	1.7	8.5	10.4	3.7	0.04
10	34.4	1.7	11.1	13.9	7.7	—
11	22.0	1.1	10.9	10.0	—	—
12	8.6	0.6	6.2	—	—	—
13	1.7	0.1	—	—	—	—
14	0.2	—	—	—	—	—
Sum	100	6.1	39.3	37.6	13.4	0.04
Total % of incomplete fusion		8	25	40	27	

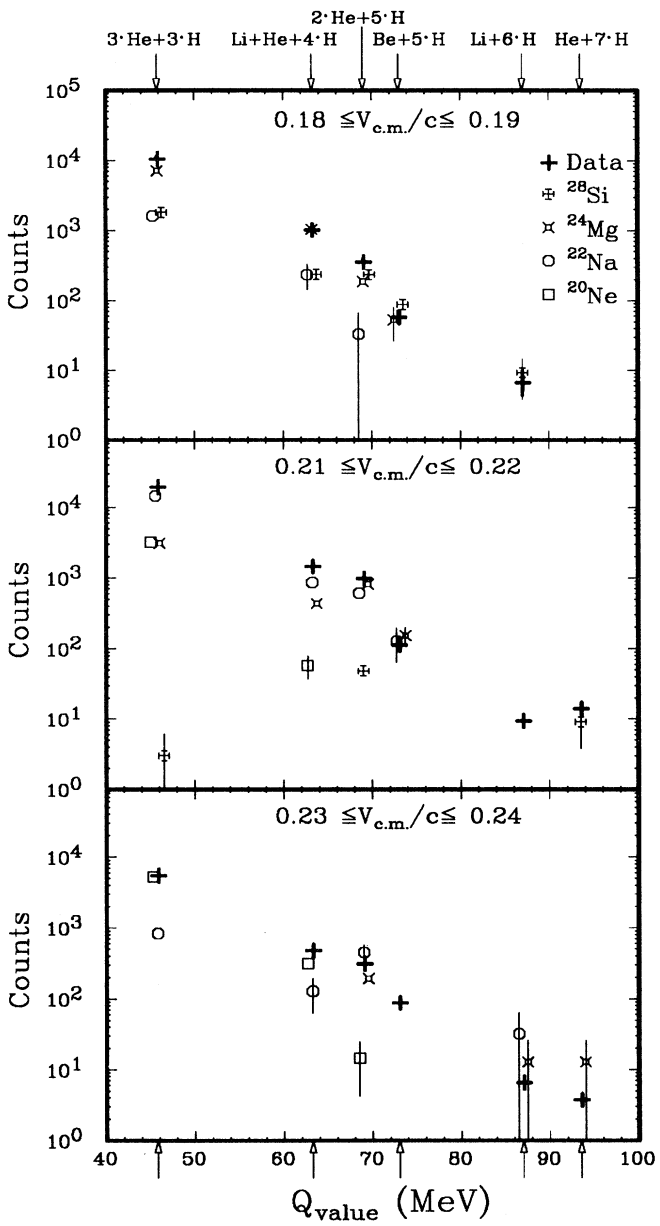

FIG. 7. Yields for initial nuclei when nine charges are detected, gated by three different regions in the velocity of the center of mass [Fig. 6(b)].

$Z_{det}=9$, and this, in turn, is correlated with the center of mass velocity of the detected fragments (see Fig. 6). By setting gates on the velocity, we should be able to select events in which the dominant primary nuclei should be either ^{24}Mg, ^{22}Na, or ^{20}Ne. A comparison of the experimental and calculated channel yields for three different gates is given in Fig. 7 where the experimental total yields for a decay channel are plotted with crosses and the calculated yields for the four primary nuclei (^{20}Ne, ^{22}Na, ^{24}Mg, and ^{28}Si) contributing to a decay channel are plotted with different symbols. The calculated yield for a given channel is the sum of the contributions from the four primary nuclei.

The experimental events for $Z_{det}=9$ are found in six different channels whose intensities vary over four orders of magnitude. As was observed in our study of the decay primary nuclei produced in peripheral reactions [4], the intensities of a particular channel decrease exponentially as the Q value for that channel becomes more negative. The calculations based on incomplete fusion and statistical decay reproduce this exponential behavior and the relative intensities of the different channels very well (see Fig. 7). Note that this agreement is not an automatic consequence of having fit the calculation to the shape of the velocity spectrum shown in Fig. 6(b). That fit ensures only that the sum of all calculated events in a given velocity bin will agree with the sum over all decay channels of all experimental events in that velocity bin.

Note further that the calculated contributions of primary nuclei contributing to a particular channel change dramatically with the center of mass velocity. For example, at the lowest velocity, ^{24}Mg is the dominant primary nucleus contributing to the 3He+3H channel, while at the highest velocity it is ^{20}Ne. At the intermediate velocity, ^{22}Na is the most important. This change in the parentage of the dominant channel is an outcome of having fit the velocity spectrum in Fig. 6(b). However, it is significant that the calculation correctly predicts the dominant channel (i.e., that it is 3He+3H) and that the predicted contributions of the different parent nuclei to the weaker channels add up in such a way to reproduce their intensities over three orders of magnitude. Examination of Fig. 7 shows that a different distribution of parent nuclei would not reproduce the exponentially varying intensities of these weaker channels. The correct prediction of the yields of the different channels, as shown in Fig. 7, is strong confirmation of the basic validity of the incomplete fusion picture.

The high velocity portion of a spectrum is, however, not always well reproduced by the fit (Fig. 6). This failing is particularly prominent for $Z_{det}=12$ and 13, and to some extent for $Z_{det}=9$. The absence of Al as a primary nucleus may be affecting the spectrum for $Z_{det}=12$ and 13. However, in order to produce a higher velocity primary nucleus, it is necessary for the projectile to capture less mass from the target while still capturing the same amount of charge. Including primary nuclei like ^{22}Mg or ^{24}Si could help reproduce the data, but at the price of introducing a more exotic reaction mechanism. However, in the case of $Z_{det}=9$, introducing ^{17}F as a primary nucleus can account for the yield at high velocities, and the production of ^{17}F (capture of one proton by the projectile) seems reasonable.

Even though the deduction of the primary nucleus distribution and the examination of the yields of different channels as a function of velocity demonstrate the general utility of the incomplete fusion analysis, there are still some shortcomings and some discrepancies with experiment. One problem is the absence of Al as a primary nucleus. There is no reason *a priori* for this absence of Al in an incomplete fusion reaction. However, we have not been compelled to include it in the fitting of the spectra for $Z_{det}=8$, 9, 10, and 11. This may be an indication that

the incomplete fusion analysis has an uncertainty of plus or minus one unit of charge in determining the primary nucleus distribution and probably at least as much regarding the mass for a given element. The same remark can be made regarding the ^{18}F. However, in this case, the high multiplicity threshold could be responsible for the small observed numbers of very light nuclei.

A final, though perhaps minor, problem is that we have no way of accounting for the observed yield of $Z_{\rm det}$=14. This yield, however, is only about 0.2% of the total incomplete fusion yield and might be possibly due to random events where the detected fragments are coming from two different collisions.

3. *Fragment energies and directional correlations*

The total charge, the laboratory velocity of the center of mass, and the composition of detected fragments have been used to characterize the reaction as the production of primary nuclei via an incomplete fusion reaction mechanism. The relative kinetic energies of the fragments and their directional correlations will now be used to evaluate different models for the decay of the primary nuclei produced in these central collisions. In this section we present the relative energies and directions of the decay fragments in their rest system, quantities that define the "shape" of the events.

The same assumptions made in the determination of the center of mass velocity of fragments in an event also enable the calculation of the individual kinetic energies of the fragments in the system in which this center of mass is at rest. The sum of these kinetic energies is the total relative kinetic energy for that event. Such energy spectra for events having $Z_{\rm det}$ = 8, 10, and 12 are shown in Fig. 8. Each spectrum includes all the channels that contribute to that particular value of the total detected charge. Note how the most probable energy and, indeed,

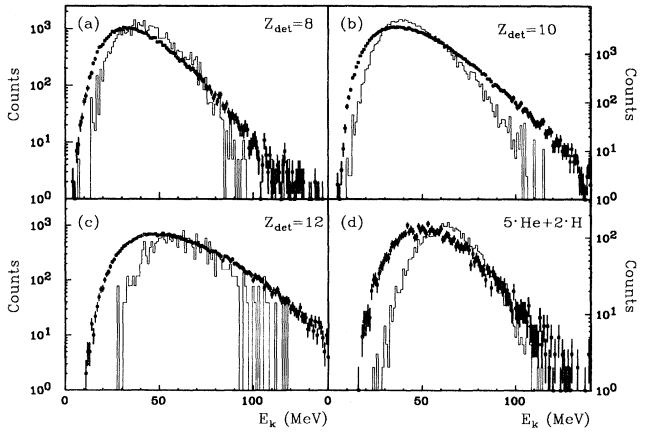

FIG. 8. Total kinetic energy spectra for (a) Z=8, (b) Z=10, and (c) Z=12 total detected charges (solid dots). GEMINI spectra are also shown as histograms. Panel (d) shows the result for the single channel 5He+2H.

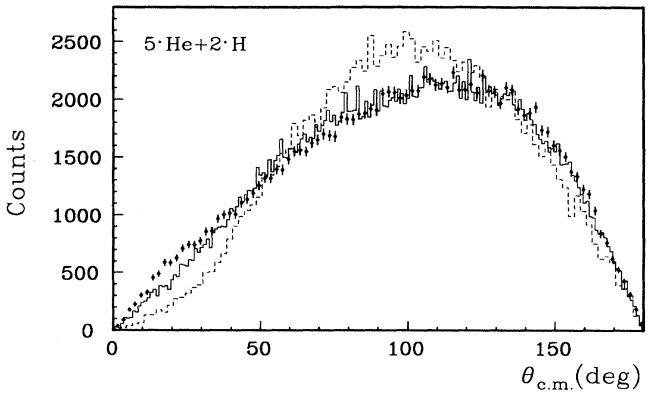

FIG. 9. Folding angles between particles for the 5He+2H events for the data (dots), GEMINI calculation (histogram), and the multifragmentation calculation (dashed histogram).

the whole spectrum shift to higher energies with each increase in the total amount of charge detected. This reflects the higher excitation energy of primary nuclei formed when more of the target mass is captured by the projectile.

In Fig. 8(d) a spectrum of relative kinetic energy is shown for a particular individual channel, 5He + 2H. In the subsequent analysis we will concentrate on the 5He + 2H channel, which the incomplete fusion analysis indicates is associated mainly with the decay of ^{24}Mg. This channel is also interesting because it is a relatively mass-symmetric channel with no heavy residual nucleus. (Although the 6He channel would seem to be a natural candidate for analysis, it was not observed in this experiment. This absence is consistent with calculations made with GEMINI, which indicated that the 6He channel had an intensity before filtering of only 1% of the 5He + 2H channel and a negligible yield after filtering.)

A straightforward way to look at directional correlations is to plot the opening (or folding) angle between pairs of particles [1]. For this analysis the vectors representing the directions of each fragment are calculated in the rest system of the fragments making up the channel. For seven particles there are 21 different angle pairs for each event. (Although it is possible to consider angle pairs separately between Z=1 particles only, Z=2 particles only, or between Z=1 and Z=2 particles, all particles were treated alike in this analysis.) The spectrum of experimental folding angles thus obtained for the 5He + 2H channel is shown in Fig. 9 (dots). It is qualitatively similar in shape to that observed for the 4He channel in the decay of ^{16}O [4,7,8].

The energies and directions of the particles in an event can be analyzed simultaneously (as opposed to separately, as in Figs. 8 and 9) by defining sphericity and coplanarity coordinates for each event. The sphericity and coplanarity coordinates are derived from the eigenvalues of the kinetic flow tensor (evaluated in the rest system of the fragments), as described in Ref. [9]. A two-dimensional scatter plot of sphericity and coplanarity coordinates for 500 events in the 5He + 2H channel is

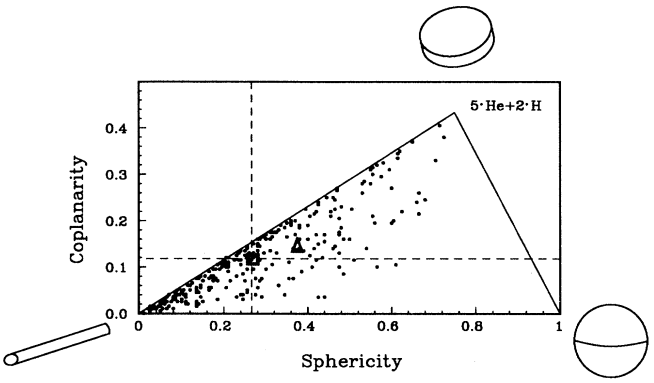

FIG. 10. Two hundred experimental data points are plotted in the sphericity-coplanarity plane. Their average value is shown by the intersection of the dashed lines. The three extreme cases are shown and correspond to the three corners of the triangle. Also shown are the centroids for the statistical calculation (square) and the multifragmentation calculation (triangle).

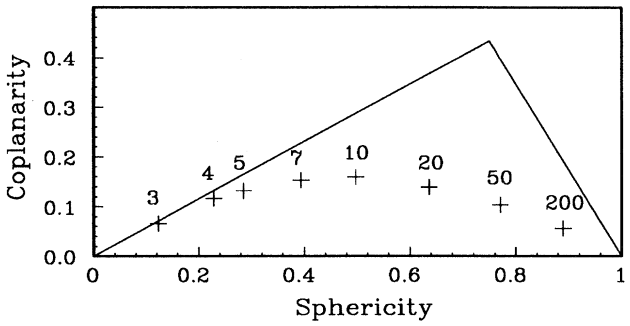

FIG. 11. Variation with the number of particle of the mean value in the sphericity-coplanarity plane for events with randomly chosen angles for the particles.

shown in Fig. 10. The events are distributed broadly over the sphericity-coplanarity plane. The average value of sphericity and coplanarity for all 5400 events is indicated by the intersection of the dashed lines.

The location of an event in the sphericity-coplanarity plane has a simple geometrical interpretation, which is indicated in Fig. 10. Events near the origin have a rodlike shape. Thus, all particle vectors are contained back to back in a long narrow cylinder. Events with a maximum coplanarity of 0.43 have a disklike shape, with the vectors distributed uniformly in a plane, while events with a maximum sphericity of 1.0 have vectors of equal length and equal angular spacing.

It is important to point out for the following comparisons with models that the average sphericity and coplanarity is influenced by the number of particles in an event. An extreme example is three particles. In this case the event must lie along the boundary line connecting the origin with the maximum value of the coplanarity. This is because conservation of momentum requires that all three momentum vectors be coplanar. For a larger number of particles, the location of an event will be governed, to some extent, by phase space. For example, there are many ways to chose four vectors that are rodlike or disklike, but only one way to orient them to achieve unit sphericity. These particle-number and phase-space considerations are illustrated in Fig. 11, which shows the average sphericity and coplanarity calculated for ensembles of identical fragments having identical energies but orientations chosen at random in the rest system of each event. (This illustrative calculation is not filtered by the experiment.) Large average sphericities are obtained only for systems with large numbers of particles. For systems with small numbers of particles, the effects on the average sphericity are quite significant, as can be seen by comparing the values for five and seven particles.

The predictions of GEMINI for the relative kinetic energies are shown in Fig. 8. The statistical model prediction is quite good for the three different cases shown. However, for $Z_{\rm det}$=12 and the 5He+2H channel, Figs. 8(c) and 8(d), the calculation is shifted to higher energies compared to the experimental data. These calculations have been made with primary nuclei having a single excitation energy and laboratory velocity as given by the incomplete fusion model as done in the velocity analysis. If this assumption were relaxed and a distribution of excitation energies used, it would probably be possible to reproduce (i.e., fit) the relative kinetic energy spectra more closely.

The folding angle spectrum predicted by the statistical model is compared to the data in Fig. 9 (solid curve). The agreement is good, overall. The main discrepancy is that GEMINI slightly underpredicts the number of small opening angles. The predicted average sphericity and coplanarity is show in Fig. 10 (square). In general GEMINI reproduces the experimental data rather well.

E. Summary on the incomplete fusion and statistical decay

Incomplete fusion followed by statistical decay have been used to reproduce experimental center of mass velocities. We have shown that with a small set of primary nuclei, coming from the fusion of the projectile with part of the target, it is possible to fit the center of mass velocities for different total detected charge (Fig. 6). Furthermore, for a total detected charge of 9, channel yields are well reproduced by the incomplete fusion plus statistical decay analysis, whatever the gate on the center of mass velocity (Fig. 7).

Folding angles as well as sphericity-coplanarity plots were performed for a specific channel: 5He+2H. The comparisons with the statistical calculation have shown a good agreement for both plots (Figs. 9 and 10).

Angular momentum was taken into account in the calculations according to the prescriptions of Ref. [5]. We checked the influence of the angular momentum by performing the same calculations with different maximum angular momentum. It was found that the folding angle spectrum was not sensitive to angular momentum for values up to the ones that were used (see Sec. III B), but

would show a drastically different pattern for higher angular momentum. Two peaks would then appear in the spectrum, at lower and higher relative angles, signaling the presence of an initial binary split, through a rodlike shape. As for the sphericity-coplanarity plot, for zero angular momentum, the sphericity component would be very high, around 0.4, and would then decrease gradually with increasing angular momentum.

IV. MULTIFRAGMENTATION ANALYSIS

In the statistical decay calculation, particles are emitted in a series of binary splits with equilibrium reestablished after each split. Another model to which the data can be compared is the multifragmentation model, where multifragmentation is defined as the simultaneous splitting of the nucleus into three or more fragments. The kinematical model of López and Randrup [9] was used to predict the directional correlations for such a decay.

The kinematical multifragmentation model described in Ref. [9] considers a nucleus as a spherical volume containing a specified number and type of fragments in relative motion. The number and type of fragments and their total relative kinetic energy at infinity are the only input to this model, which only considers the kinematic aspects of the simultaneous breakup. The program positions the fragments at random locations in a sphere of radius slightly larger than the one of the initial bound nucleus and then calculates the Coulomb potential energy of the system. If the potential energy is larger than the total kinetic energy, a larger sphere is assumed and fragments are positioned again. If, on the other hand, the potential energy is lower than the kinetic energy, then the missing energy is shared between the fragments in the form of random velocities having a Maxwellian distribution. Thereafter the program calculates the trajectory for each fragment as determined by their mutual Coulomb repulsions. Angular momentum is not taken into account in this calculation.

The total excitation energy of the nucleus in this calculation is the sum of the potential energy, the kinetic energy, and the Q value. Note that if the system has a large amount of relative kinetic energy, which generally means a great amount of excitation energy to start with, then the decay pattern will be predominantly random. Initial velocities will be large with random directions and the Coulomb forces will have a relatively small effect on the trajectories. This is illustrated in Fig. 12 which shows three multifragmentation calculations for the decay of ^{24}Mg into the 5He+2H channel, at 30, 50, and 100 MeV of kinetic energy. The Coulomb potential energy of the system at the initial positions of all the particles in the sphere is about 22 MeV. The position in the sphericity-coplanarity plane is drastically different for these three calculations, which points out the importance of knowing the relative kinetic energy. This is not the case with the statistical decay calculation for which the shape of the event can be shown to be rather insensitive to the initial excitation energy of the system. In our case the experimental signature of multifragmentation is the effect of the Coulomb energy, or mutual Coulomb repulsion on the trajectories of the fragments as they recede from each other at the time of decay.

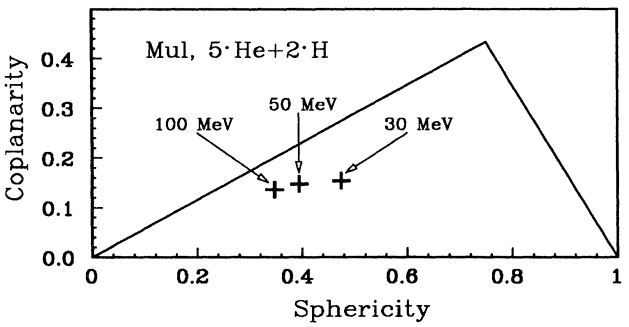

FIG. 12. Centroid in the sphericity-coplanarity plane for multifragmentation performed for 5He+2H events with 30, 50, and 100 MeV of kinetic energy.

Figure 8(d) shows that the average total relative kinetic energy of the charged particles is predicted within 10 MeV by GEMINI code (peaking about 60 MeV instead of 50 MeV for the data). This is accurate enough to be used as an input value for the multifragmentation calculation and will not alter the shape of the events. The initial conditions are thus taken with the masses and the kinetic energy given by GEMINI. The multiframentation calculation gathers and positions the charged particles, calculates the Coulomb energy, and the initial kinetic energy is obtained by substracting the Coulomb energy from the total kinetic energy given by GEMINI. Final center of mass velocities, after Coulomb repulsion, are then calculated. The velocity of the center of mass in the laboratory frame is added and the filtering applied to the event.

Figure 10 shows the average position in the sphericity-coplanarity plot for the multifragmentation calculation (triangle) as well as for the statistical calculation (square) and the data for the 5He+2H channel. The multifragmentation calculation shows a quite spherical pattern as expected from the three calculations done at fixed energy and from the average free kinetic energy from the GEMINI calculation [Figs. 12 and 8(d)], very different from the data, which exhibit a rodlike shape.

The folding angle pattern (Fig. 9, dashed histogram) is quite different from the data as well. It is centered at a lower angle which reflects the more isotropic distribution of the emitted particles of these multifragmentation events.

V. CONCLUSION

Central collision of ^{16}O + ^{12}C at 32.5 MeV/nucleon has been analyzed in terms of incomplete fusion followed by statistical decay. A decomposition of the center of mass velocity spectrum for different total detected charge events was performed and good overall results were obtained. The main channels for the incomplete fusion were found to be ^{24}Mg, ^{22}Na, and ^{20}Ne with respectively 25%, 40%, and 27% of the cross section.

Preequilibrium emission by fragments produced as a result of incomplete fusion was not considered in this analysis. In the incomplete fusion model, the fraction of the target that did not fuse with the projectile (and that could not be detected in our experiment) represents preequilibrium particles.

Folding angle and sphericity-coplanarity distributions were obtained for a specific channel, 5He+2H, and were well reproduced by a statistical decay calculation (GEMINI). The same analysis was performed with a multifragmentation code and predicts a larger sphericity for that channel due to the mutual Coulomb repulsion of the fragments emitted simultaneously in the decay. Consequently, smaller average folding angles (than for the data) were obtained. No correlation seems to be observed between the particles in the data; i.e., no Coulomb repulsion effect as expected by the multifragmentation model used. However, one should point out the limitations of the model. First of all, angular momentum is not taken into account and it has been shown that it plays an important role in lowering the sphericity given by the statistical calculation. Also, Charity *et al.* [7] have shown the importance of the nuclear final state effects, in particular the resonance scattering of two alpha particles through the ground state and the first excited states of ^{8}Be, which drastically modifies their correlation function. Furthermore, they claim that this effect works in the opposite direction to that from the Coulomb repulsion, and in the same direction as what is expected when increasing the initial angular momentum.

ACKNOWLEDGMENTS

This work was supported in part by the U.S. Department of Energy under Contract No. DE-AC03-76SF00098.

APPENDIX

The continuous energy calibrations for the phoswich detectors were obtained by combining the discrete measurements with a linearization and fitting procedure based on the characteristics of the detectors and electronics. Since the particular procedure we developed is not reported elsewhere, we describe it here.

We reproduce the bananalike pattern observed in Fig. 2 with a parametrized calculation, and then adjust the free parameters to reproduce the calibration points. In order to apply this method we need to know the characteristics of the signal produced when a particle is stopped in the detector. The physical characteristics of the phoswich detectors and the electronics are described in Ref. [2], with the exception that the thickness of the ΔE layer was reduced to 0.4 cm. The decay times of the two plastics are, respectively, $\tau_{\rm fast}$=1.8 ns and $\tau_{\rm slow}$=225 ns for the fast and slow components. The relative amount of light from each plastic layer has been calculated by an energy-loss code for scintillation emission, weighted by the equivalent anthracene light output.

Assuming a negligible rise time of the signal compared to the gate widths the output signal can be written as

$$\mathcal{O}_{\mathcal{S}} = \frac{e_1}{\tau_{\rm fast}} e^{-\frac{t}{\tau_{\rm fast}}} + \mathcal{R}\frac{e_2}{\tau_{\rm slow}} e^{-\frac{t}{\tau_{\rm slow}}}, \tag{A1}$$

where e_1 and e_2 are the total light obtained by the energy-loss code for the two plastics of thicknesses used in the experiment, $\mathcal{R}$ is the ratio of the equivalent anthracene light output of the two plastics, and $\tau_{\rm fast}$ and $\tau_{\rm slow}$ are the respective decay times.

Assuming that the short gate length and the long gate length are much larger than, respectively, the fast and slow signal characteristic decay times, $\tau_{\rm fast}$ and $\tau_{\rm slow}$, the integrated signal components in the short and the long gates, ($\mathcal{S}_{\mathcal{G}}$) and ($\mathcal{L}_{\mathcal{G}}$), can be expressed as follows:

$$\mathcal{S}_{\mathcal{G}} = a_{\rm short}[\mathcal{F}(z)e_1 + \epsilon(z)\mathcal{R}e_2] + b_{\rm short}, \tag{A2}$$

$$\mathcal{L}_{\mathcal{G}} = a_{\rm long}[\mathcal{F}(z)e_1 + \mathcal{R}e_2] + b_{\rm long}, \tag{A3}$$

where $a_{\rm short}$ and $a_{\rm long}$ are factors that take care of the photomultiplier gains (for the linear part) as well as the analog-to-digital-converter (ADC) gains; $\mathcal{F}$(z) is a factor meant to take into account the nonlinearity of the photomultiplier and depends on the detected particle. Particles that lose a lot of energy in the first layer produce a large amount of light in a very short time (a few nanoseconds), which may saturate the photomultiplier. No such effect is expected for the slow component, since the light is much more spread in time. $b_{\rm short}$ and $b_{\rm long}$ are the values of the $\mathcal{S}_{\mathcal{G}}$ and $\mathcal{L}_{\mathcal{G}}$ components when no particle is detected (i.e., the electronic pedestals), and ϵ is the fraction of the slow component integrated in the short gate. The quantity ϵ, which depends on the nature of the particle, can be written as

$$\epsilon = 1 - e^{\frac{t_{\rm eff}}{\tau_{\rm slow}}}. \tag{A4}$$

Even if the experimental gate width is known to be 40 ns, the effective length, $t_{\rm eff}$, i.e., the time during which the signal is integrated, is smaller. In our experiment the short gate was the same for every detector (a common start and a common stop), and since slow and fast moving particles were detected, the straggling in arrival time at detectors might have been quite important. For example, protons are expected to have higher velocity, on the average, than carbon. The factor ϵ is thus dependent on the nature of the particle. The effective length of time during which the signal is integrated, $t_{\rm eff}$, was adjusted for each particle type to best fit the data.

Because part of the slow component is integrated in the short gate, the $\mathcal{S}_{\mathcal{G}}$ component does not drop to zero when the particle energy loss in the first layer goes to zero. The fraction of the slow component integrated in the short gate defines the curvature of the identification lines.

A way to find the ratio of the equivalent anthracene light output of the two plastics, R, is to use two points of known energy for a given particle. One can be the intersection of the line with the backbone line and the other a calibration point. The $\mathcal{L}_{\mathcal{G}}$ components $\mathcal{L}_{\mathcal{G}}^{(1)}$ and $\mathcal{L}_{\mathcal{G}}^{(2)}$ for the two points can be written as

$$\mathcal{L}_{\mathcal{G}}^{(1)} = a_{\text{long}}\mathcal{F}(z)e_1^{(1)} + b_{\text{long}} \tag{A5}$$

for the particle at the loci point and

$$\mathcal{L}_{\mathcal{G}}^{(2)} = a_{\text{long}}[\mathcal{F}(z)e_1^{(2)} + \mathcal{R}e_2^{(2)} + b_{\text{long}} \tag{A6}$$

for the calibration point. Through the difference of the two previous equations we find

$$\mathcal{R} = \frac{\mathcal{L}_{\mathcal{G}}^{(2)} - \mathcal{L}_{\mathcal{G}}^{(1)} - a_{\text{long}}\mathcal{F}(z)[e_1^{(2)} - e_1^{(1)}]}{e_2^{(2)}}, \tag{A7}$$

where $\mathcal{L}_{\mathcal{G}}^{(2)}$ and $\mathcal{L}_{\mathcal{G}}^{(1)}$ are given by the experimental data points, a_{long} and $\mathcal{F}(z)$ are found by fitting the loci points, and $e_1^{(2)}$, $e_1^{(1)}$, and $e_2^{(2)}$ are given by the energy-loss code.

$\mathcal{R}$ has been determined by first using proton data and then alpha particle data. The values found were

$$\mathcal{R} = 0.31 \tag{A8}$$

from the proton measurement and

$$\mathcal{R} = 0.285 \tag{A9}$$

from the alpha particle measurement.

A mean value of 0.295 was used. This ratio $\mathcal{R}$ corresponds to an equivalent anthracene light output of 20% for the NE-115 if we believe the well-known value of 68% for the BC-404 plastic. A similar result was found by Meijer *et al.* using a different method [10]. Their final value was 22% of anthracene light output. Both values are quite close to Nuclear Enterprise specification of 25%, but disagree with the 35% measured by Bantel *et al.* [11].

After fitting the data with smooth curved lines, one for every type of fragment, we checked how well the energy of the calibration points agreed with the experimental data. An agreement better than 10% was obtained when comparing the calibration data for the set of all detectors with the energies extracted from the simulation.

TABLE IV. Fitting parameters for the identification plot. See text.

					Gate width t_{eff} (ns) Fraction factor $\mathcal{F}$				
a_{short}	a_{long}	b_{short}	b_{long}	p	He	Li	Be	B	C
1.43	0.5	20	34	31	25	29	25	22	19
				1	1	1	0.82	0.7	0.62

A typical fit to the data is shown in Fig. 2 and the corresponding fitting parameters are listed in Table IV. The pedestals b_{short} and b_{long} are obtained by the intersection of the backbone line and the upper straight line created by detected particles that missed the first layer. The factors a_{short} and a_{long} are set to fit the intersection of the proton line and the alpha line with the backbone, for which no saturation is expected [$\mathcal{F}(z)$=1]. The effective width of the short gate is chosen to reproduce the curvature of the identification lines and the saturation factors $\mathcal{F}(z)$ to keep the intersections with the backbone at the right values.

Such fits were made for every detector including the position-sensitive detectors. This method provides a better understanding of the identification plots and gives a good calibration that can be applied to the whole range of energy.

[1] B.A. Harmon, J. Pouliot, J.A. López, J. Suro, R. Knop, Y. Chan, D.E. DiGregorio, and R.G. Stokstad, Phys. Lett. B **235** 1990 (234).

[2] J. Pouliot, Y. Chan, A. Dacal, A. Harmon, R. Knop, M.E. Ortiz, E. Plagnol, and R.G. Stokstad, Nucl. Instrum. Methods A **270**, 69 (1988).

[3] H.R. Schmidt, M. Bantel, Y. Chan, S.B. Gazes, S. Wald, and R.G. Stokstad, Nucl. Instrum. Methods A **242**, 111 (1985).

[4] J. Pouliot, Y. Chan, D.E. DiGregorio, B.A. Harmon, R. Knop, C. Moisan, R. Roy, and R.G. Stokstad, Phys. Rev. C **43**, 735 (1991).

[5] R. Bass, Nucl. Phys. **A231**, 45 (1974); Phys. Rev. Lett. **39**, 265 (1977).

[6] R.J. Charity *et al.*, Nucl. Phys. **A483**, 371 (1988).

[7] R.J. Charity *et al.*, Phys. Rev. C **46**, 1951 (1992).

[8] D. Doré *et al.*, Nucl. Phys. **A545**, 363c (1992).

[9] J.A. López and J. Randrup, Nucl. Phys. **A491**, 477 (1989).

[10] R.J. Meijer, A. van den Brink, E.A. Bakkum, P. Decowski, K.A. Griffioen, and R. Kamermans, Nucl. Instrum. Methods A **264**, 285 (1988).

[11] M. Bantel, R.G. Stokstad, Y.D. Chan, S. Wald, and P.J. Countryman, Nucl. Instrum. Methods **226**, 394 (1984).

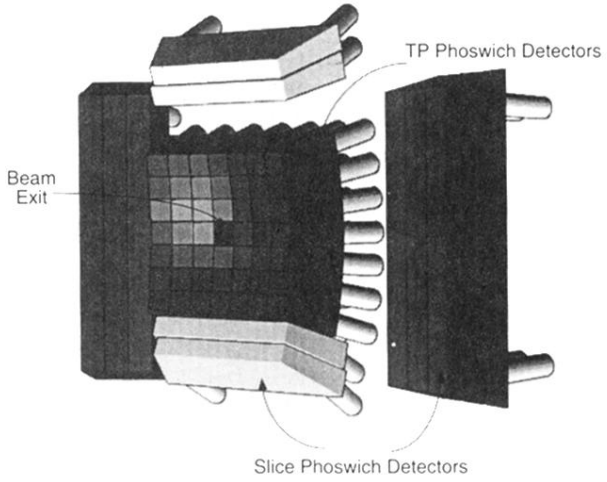

FIG. 1. Plastic phoswich detector array for light charged particles. The slices are positioned symmetrically about the 47-detector array. The top and right slice detectors have been shifted in the drawing to reveal the central cubic array.